Cloud Liquid Water and Ice Content Retrieval by Multiwavelength Radar

NICOLAS GAUSSIAT AND HENRI SAUVAGEOT

Université Paul Sabatier, Observatoire Midi-Pyrénées, Laboratoire d'Aérologie, Toulouse, France

ANTHONY J. ILLINGWORTH

Department of Meteorology, University of Reading, Reading, United Kingdom

(Manuscript received 25 March 2002, in final form 15 March 2003)

ABSTRACT

Cloud liquid water and ice content retrieval in precipitating clouds by the differential attenuation method using a dual-wavelength radar, as a function of the wavelength pair, is first discussed. In the presence of non-Rayleigh scatterers, drizzle, or large ice crystals, an ambiguity appears between attenuation and non-Rayleigh scattering. The liquid water estimate is thus biased regardless of which pair is used. A new method using three wavelengths (long λ_l, medium λ_m, and short λ_s) is then proposed in order to overcome this ambiguity. Two dual-wavelength pairs, (λ_l, λ_m) and (λ_l, λ_s), are considered. With the (λ_l, λ_m) pair, ignoring the attenuation, a first estimate of the scattering term is computed. This scattering term is used with the (λ_l, λ_s) pair to obtain an estimate of the attenuation term. With the attenuation term and the (λ_l, λ_m) pair, a new estimate of the scattering term is computed, and so on until obtaining a stable result. The behavior of this method is analyzed through a numerical simulation and the processing of field data from 3-, 35-, and 94-GHz radars.

1. Introduction

The radiative balance of the atmosphere is very sensitive to the distribution of ice and liquid water in clouds (Stephens et al. 1990; Cess et al. 1996). The microphysical features of clouds are not well known because of the lack of observational data, and, in order to collect such data, space missions are planned. However, reliable methods and algorithms to be used for ice and liquid water retrieval are not fully available.

Single-radar reflectivity measurements do not enable the determination of the liquid water content profile of clouds. Two cases have to be considered: liquid and mixed-phase clouds. Most often, the entirely liquid clouds are made up of a high concentration of small droplets, corresponding to the main part of the liquid water content and controlling the radiative transfer with, in addition, a low concentration of large droplets, or drizzle, which only make a small contribution to the liquid water content of the cloud. In ice clouds, the presence of updrafts sometimes induces the development of a liquid phase, in the form of small droplets, mixed with ice crystals having a comparatively larger size (Young 1993). In both cases, the radar reflectivity is dominated by the largest (non-Rayleigh) scatterers, drizzle, or crystals, so that there is no relation between the radar reflectivity factor and the liquid water content or the optical thickness of the cloud (Sauvageot and Omar 1987; Fox and Illingworth 1997).

The most promising way to quantitatively observe the liquid water content in clouds seems to be the differential-attenuation-based dual-wavelength radar method. This method was proposed to observe the liquid water content in single-phase clouds (Atlas 1954; Martner et al. 1993; Hogan et al. 1999), the liquid water and ice content in mixed-phase clouds (Gosset and Sauvageot 1992; Vivekanandan et al. 1999), or the liquid water content in rain (Eccles and Muller 1971).

The principle of the method is the following: the large scatterers (drizzle drops or ice crystals), which dominate the radar reflectivity, have a negligible effect on the attenuation, whereas the small droplets, responsible for the liquid water content, dominate the attenuation. From measurements of the range reflectivity profiles for two wavelengths, one being strongly attenuated, the other weakly so, the differential attenuation can be determined and, from it, the cloud liquid water content deduced (cf. section 2). The method works, provided that all of the scatterers are small enough to satisfy the Rayleigh scattering conditions, for which the radar reflectivity factor Z is independent from the wavelength λ. In the presence of non-Rayleigh scatterers, an ambiguity is observed between the differential attenuation and a reflectivity difference appearing because Z is no longer independent from λ.

Corresponding author address: Dr. Henri Sauvageot, Université Paul Sabatier (Toulouse III), Centre de Recherches Atmosphériques, Campistrous, 65300 Lannemezan, France.
E-mail: sauh@aero.obs-mip.fr

The aim of this paper is to discuss the difficulty of implementing the dual-wavelength differential attenuation method in the presence of non-Rayleigh scatterers and to propose a new method using an additional wavelength in order to retrieve the differential attenuation.

Dual-wavelength radar algorithms have also been proposed for the sizing of ice crystals in cirrus clouds (Hogan and Illingworth 1999; Hogan et al. 2000), or hailstones in convective storms (Atlas and Ludlam 1961; Eccles and Atlas 1973). In this context, the wavelength pairs are chosen in such a way that the particles to be sized at the higher frequency are in the Mie (or non-Rayleigh) scattering region (Deirmendjian 1969). The sizing depends on the reflectivity difference as a function of the wavelength, since, for the Mie scattering region, the reflectivity is lower than for the Rayleigh scattering. Of course, these algorithms assume that differential attenuation is negligible, because if not, an ambiguity also appears between Mie scattering and differential attenuation. In the present paper, the use of the concept of the triple-wavelength radar for particle sizing is also considered.

2. Theory

The reflectivity factor $Z_{m,\lambda}$ of a cloud measured with a radar of wavelength λ, at distance r, depends on the equivalent reflectivity factor of the scatterers $Z_{e,\lambda}$ and on the attenuation along the radar-target propagation path:

$$Z_{m,\lambda} = Z_{e,\lambda}\, 10^{-0.2 \int_0^r A_\lambda(u)\, du}, \tag{1}$$

where A_λ is the one-way attenuation factor for cloud and gas, assuming that there is no precipitation on the path other than drizzle and ice crystals, as discussed above; Z is in $\mathrm{mm}^6\ \mathrm{m}^{-3}$ and A in decibels per kilometer.

In this paper, four radar frequency bands—S (f = 3 GHz, λ = 10 cm), X (f = 9.4 GHz, λ = 3.2 cm), Ka (f = 35 GHz, λ = 0.86 cm), and W (f = 94 GHz, λ = 0.32 cm), where f is the frequency—are considered.

For the Rayleigh scattering, the radar reflectivity factor is $Z = \int D^6 N(D)\, dD$, where $N(D)$ is the size distribution of the equivalent spherical diameter D of the scatterers, which means that Z is independent of λ.

The equivalent reflectivity factor $Z_{e,\lambda}$ is related to the ordinary reflectivity factor (e.g., Sauvageot 1992) by

$$Z_{e,\lambda} = \frac{|K(\lambda)|^2}{|K_w(\lambda, 0)|^2} Z, \tag{2}$$

where $|K_w(\lambda, 0)|^2$ is the dielectric factor for liquid water at 0°C and $|K(\lambda)|^2$ is the actual dielectric factor of the scatterers. For example, $|K_w|^2 = 0.934$ for the S band, 0.930 for the X band, 0.881 for the Ka band, and 0.686 for the W band at 0°C (e.g., Ray 1972; Meneghini and Kozu 1990).

From (1) and (2),

$$10 \log(Z_{m,\lambda}) = 10 \log(Z) + 20 \log|K(\lambda)/K_w(\lambda, 0)| - 2 \int_0^r A_\lambda(u)\, du. \tag{3}$$

The dielectric factor depends on the thermodynamic phase and temperature of the scatterers. For liquid water, the dielectric factor is weakly dependent on the temperature and it can be written that $20 \log(|K(\lambda)|/|K_w(\lambda, 0)|) \cong 0$ (e.g., Ray 1972). For ice, the dielectric factor is almost independent from the temperature and wavelength, with $|K(\lambda)|^2 = 0.176$ (for a density $\rho = 0.92$ g cm^{-3}), but it does depend on the density for air–ice mixture.

The differential-attenuation dual-wavelength radar methods consider the dual-wavelength ratio (DWR) defined for a wavelength pair (λ_s, λ_l) as

$$\mathrm{DWR} = 10 \log\left(\frac{Z_{m,\lambda_l}}{Z_{m,\lambda_s}}\right), \tag{4}$$

where the subscripts s and l stand for short and long wavelength, respectively.

In the absence of non-Rayleigh scatterers, $Z_{e,\lambda_l} = Z_{e,\lambda_s}$. Using (3) in (4) then gives

$$\mathrm{DWR} = 2 \int_0^r (A_{\lambda_s} - A_{\lambda_l})\, du + R_{\lambda_l,\lambda_s}, \tag{5}$$

with

$$R_{\lambda_l,\lambda_s} = 20 \log\left(\frac{|K(\lambda_l)K_w(\lambda_s, 0)|}{|K(\lambda_s)K_w(\lambda_l, 0)|}\right). \tag{6}$$

For liquid water clouds, $R_{\lambda_1,\lambda_s} \cong 0$. For ice clouds, $R_{\lambda_1,\lambda_s} = -0.23$ dB for the (λ_S, λ_{Ka}) and (λ_X, λ_{Ka}) wavelength pairs, and -1.27 dB for the (λ_S, λ_W) and (λ_X, λ_W) pairs. For Rayleigh scattering, DWR is thus equal, within a constant, to the cumulative differential attenuation along the radar-target path.

In the Rayleigh domain of approximation, the attenuation by liquid water is proportional to the liquid water content M_w. Neglecting attenuation by ice (e.g., Gosset and Sauvageot 1992),

$$A_\lambda = C_\lambda M_w, \tag{7}$$

where C_λ is the attenuation coefficient. For a radial path between r and $r + \Delta r$, over which M_w is assumed homogeneous and uniform, the variation of DWR is, from (5) and (7) and after correction for atmospheric gas attenuation,

$$\frac{\Delta \mathrm{DWR}}{\Delta r} = 2(C_{\lambda_s} - C_{\lambda_l}) M_w(r), \tag{8}$$

where C_{λ_s} and C_{λ_l} are the attenuation coefficients for water clouds at λ_s and λ_l, respectively. The cloud liquid water content is thus proportional to the DWR variation along the radial path, namely,

$$M_w(r) = \frac{1}{2(C_{\lambda_s} - C_{\lambda_l})} \frac{\Delta \text{DWR}}{\Delta r}. \quad (9)$$

Knowing $M_w(r)$, it is possible to compute an estimate of the ice content $M_i(r)$ from the reflectivity profile using empirical Z–M_w, Z–M_i relationships. This algorithm applies to mixed and to warm clouds. It is not applicable to ice clouds because the attenuation by ice crystals is too small to produce an accurately measurable differential attenuation. What can be used in ice-only clouds are the conventional Z–M_i algorithm or a sizing dual-wavelength algorithm.

In the presence of non-Rayleigh scatterers, that is, in the Mie scattering region, the radar reflectivity factor is no longer the sixth moment of the scatterer size distribution and depends on the wavelength. For a distribution of non-Rayleigh scatterers, it can be written (e.g., Sekelsky et al. 1999)

$$Z_{e,\lambda} = \frac{10^{12}\lambda^4}{4\pi^4}|K_w(\lambda)|^2 \int_0^\infty \xi_b(D, \lambda, \rho) D^2 N(D)\, dD, \quad (10)$$

where ξ_b is the backscattering efficiency (or normalized radar backscattering cross section), that is, $\xi_b = 4\sigma_b/(\pi D^2)$, with D in millimeters, λ in meters, and Z in mm^6 m^{-3} (e.g., Ulaby et al. 1981, p. 296). Here, ξ_b is a function of D, λ, particle density ρ, and shape. In the present study, it is assumed that the scatterers can be approximated by a spherical shape. For liquid water, the density is constant, whereas for the ice particles, it is assumed (Brown and Francis 1995) that

$$\rho(D) = \begin{cases} 0.916 \text{ g cm}^{-3} & \text{for } D < 0.1 \text{ mm} \\ 0.0706 D^{-1.1} \text{ g cm}^{-3} & \text{for } D > 0.1 \text{ mm}. \end{cases} \quad (11)$$

Here, ξ_b is computed using the algorithm of Deirmendjian (1969). The size distribution of the scatterers is assumed to be exponential, namely, $N(D) = N_0 \exp[-(3.67)D/D_0]$, where N_0 is a parameter and D_0 is the mean volume diameter. Using (10), the ratio of the effective reflectivity factors is

$$10 \log\left(\frac{Z_{e,\lambda_l}}{Z_{e,\lambda_s}}\right) = F_{\lambda_l,\lambda_s}(D_0) + R_{\lambda_l,\lambda_s}, \quad (12)$$

with

$$F_{\lambda_l,\lambda_s}(D_0) = 10 \log\left[\frac{\lambda_l^4 \int_0^\infty \xi_b(D, \lambda_l) D^2 e^{-3.67D/D_0}\, dD}{\lambda_s^4 \int_0^\infty \xi_b(D, \lambda_s) D^2 e^{-3.67D/D_0}\, dD}\right].$$

In the presence of non-Rayleigh scatterers, DWR is thus a function of the attenuation and of D_0, namely,

$$\text{DWR} = F_{\lambda_l,\lambda_s}(D_0) + A_d + R_{\lambda_l,\lambda_s}, \quad (13)$$

where A_d is the differential attenuation, that is,

$$A_d = 2 \int_0^r (A_{\lambda_s} - A_{\lambda_l})\, du. \quad (14)$$

3. Ambiguity between attenuation and scattering

Figure 1 presents the variations of the non-Rayleigh term F_{λ_l,λ_s}, as a function of D_0, for four pairs of wavelengths and for liquid and ice scatterers. The non-Rayleigh term increases with the radioelectric size, $\chi = \pi D/\lambda$, of the scatterers, that is, when D_0 increases and λ decreases. For a same D_0, the non-Rayleigh term is smaller for ice than for liquid water. The results are not sensitive to the choice of λ_S and λ_X (and so for the wavelength between λ_s and λ_x) as the longer wavelength, but using the Ka band as short wavelength rather than the W band results in a marked decrease of the non-Rayleigh term.

The differential attenuation algorithm described in section 2 can be considered as reliable when $F_{\lambda_l,\lambda_s}(D_0)$, the non-Rayleigh contribution to ΔDWR, is negligible or not too large with respect to the cumulative differential attenuation $A_d \Delta r$. To discuss this point, two aspects have to be considered. First, M_w fluctuates along a radial and the cumulative differential attenuation depends on the length of the integration path. Second, $F_{\lambda_l,\lambda_s}(D_0)$ depends on the particular value of $Z_{e,\lambda}$ in the range bin in which it is computed. Generally, $F_{\lambda_l,\lambda_s}(D_0)$ decreases with $Z_{e,\lambda}$. Moreover, as discussed by Vivekanandan et al. (1999), ΔDWR is not affected by a Mie scattering if two Rayleigh range bins with low $Z_{e,\lambda}$ are available at each end of the segment Δr where ΔDWR is derived. However, in field cases, such an opportunity may not arise and more general conditions compatible with a sampling process of radials with a constant Δr have to be used.

In order to illustrate the contribution of D_0 and A_d to the dual-wavelength ratio, an integration path of length equal to 5000 m with an attenuating cloud liquid water content of 0.2 g m^{-3}, that is, an integrated liquid water amount of 1000 g m^{-2}, is considered. We have computed the corresponding values of the cumulative integrated differential attenuation and maximum D_0, such as $F_{\lambda_l,\lambda_s}(D_0)$ be equal to 10% of A_d. Table 1, where the results are given, suggests that the condition $F_{\lambda_l,\lambda_s}(D_0) < 0.1Ad$ is not very frequently observed in nature, because drizzle is very common in warm clouds and ice crystals are large in mixed clouds. That is why it is relevant to look for an algorithm able to overcome the non-Rayleigh scattering problem for liquid water retrieval.

4. Triple-wavelength algorithm

To remove the ambiguity between $F_{\lambda_l,\lambda_s}(D_0)$ and A_d in the presence of a warm or mixed cloud, including non-Rayleigh scatterers, a triple-wavelength approach is proposed.

a. Principle

A triple-wavelength radar is considered. The three wavelengths are noted λ_l, λ_m, and λ_s, where the sub-

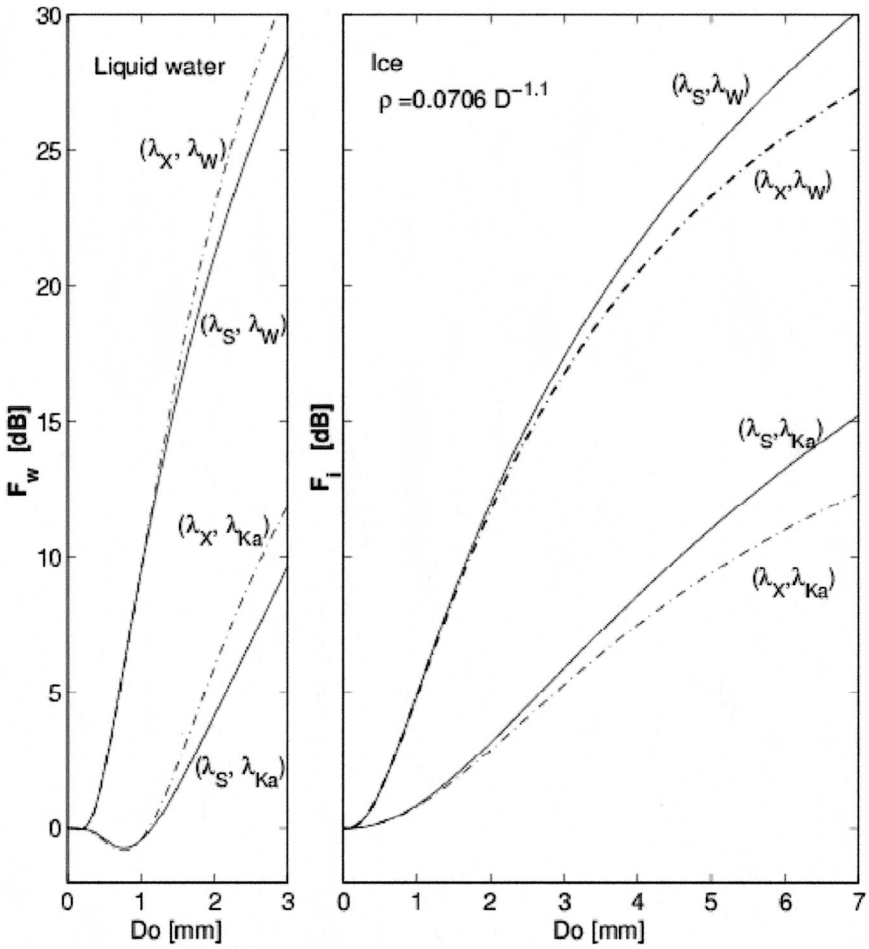

FIG. 1. Variation of the non-Rayleigh scattering term $F_{\lambda_l,\lambda_s}(D_0)$ for water and for ice, written F_w and F_i, respectively, as a function of the mean volume diameter D_0. Here λ_s, λ_x, λ_{Ka}, λ_w are wavelengths for S, X, Ka, and W bands, respectively; ρ is the density in g cm^{-3}, with D in mm.

scripts l, m, and s stand for long, medium, and short, respectively. In the present work, λ_l corresponds to an S, C, or X band; λ_m to a Ka band; and λ_s to a W band. Using the range distribution of reflectivities observed with such a radar, a linear system of two independent equations similar to (13) can be written:

$$\mathrm{DWR}_{\lambda_l,\lambda_m} = F_{\lambda_l,\lambda_m}(D_0) + 2\int_0^r (A_{\lambda_m} - A_{\lambda_l})\,du + R_{\lambda_l,\lambda_m}, \quad (15)$$

$$\mathrm{DWR}_{\lambda_l,\lambda_s} = F_{\lambda_l,\lambda_s}(D_0) + 2\int_0^r (A_{\lambda_s} - A_{\lambda_l})\,du + R_{\lambda_l,\lambda_s}. \quad (16)$$

Differential attenuation for the (λ_l, λ_m) pair is much smaller than that of the (λ_l, λ_s) pair. Assuming, in a first step, that the cumulative differential attenuation is negligible, (15) is used to compute D_0 by solving $\mathrm{DWR}_{\lambda_l,\lambda_m} = F_{\lambda_l,\lambda_m}(D_0) + R_{\lambda_l,\lambda_m}$ for each range bin. From this profile of D_0, the non-Rayleigh scattering term of (16) can be computed. Then a first estimate of the cumulative differential attenuation for the (λ_l, λ_s) pair is obtained in each range bin from the difference, in (16), between the $\mathrm{DWR}_{\lambda_l,\lambda_s}$ observed and the $F_{\lambda_l,\lambda_s}(D_0)$ computed.

The cumulative differential attenuation first neglected in (15) for the (λ_l, λ_m) pair can now be deduced from the cumulative differential attenuation computed for the (λ_l, λ_s) pair. In fact, for an attenuating medium made up of water droplets satisfying the Rayleigh approximation conditions, it is possible to write from (7)

$$(A_{\lambda_m} - A_{\lambda_l}) = k(A_{\lambda_s} - A_{\lambda_l}), \quad (17)$$

where the coefficient k ($\cong$0.19; see Table 1) is dimensionless and depends on the temperature.

Taking into account the attenuation term in (15) to compute a better estimate of the non-Rayleigh term $F_{\lambda_l,\lambda_m}(D_0)$, a new profile of the cumulative differential attenuation can be obtained and so on. The iterative process ends when the profile of cumulative differential attenuation is stable.

TABLE 1. (upper) Difference between attenuation coefficients by liquid water at 0°C for the four wavelength pairs and values of factor k of (17); (lower) total differential attenuation and corresponding D_{0max} for LWP = 1000 g m^{-2} and $F(D_0) < 0.1\ A_d$.

Wavelength pair	(λ_S, λ_W)		(λ_S, λ_{Ka})	(λ_X, λ_W)		(λ_X, λ_{Ka})
$C_{\lambda_s} - C_{\lambda_f}$ at 0°C (dB g m^{-3} km^{-1})	5.34		1.05	5.25		0.97
k at 0°C in (17)		0.20			0.18	
$2\int_0^\infty (A_{\lambda_s} - A_{\lambda f})\ dr$ (dB)	10.70		2.10	10.50		1.90
D_{0max} in ice (mm)	0.44		0.53	0.42		0.51
D_{0max} in water (mm)	0.41		0.41	0.40		0.40

The profile of M_w is obtained by taking the derivative of the cumulative differential attenuation with respect to the distance, assuming that M_w is proportional to the differential attenuation. To obtain the ice content profile, the relation between M_i and the ice particle size distribution $N(D)$ is first considered, that is, $M_i = (\pi/6) \int D^3 \rho(D) N(D) dD$. This relation depends on N_0 and D_0, the parameters of $N(D)$. The profile of D_0 is given by the algorithm, as explained above, and the N_0 profile is obtained from the reflectivity factor profile at λ_l (unattenuated) and from the D_0 profile by inverting the analytical relation $Z_{\lambda_l} = f(D_0, N_0)$. The same derivation is used by Sekelsky et al. (1999). The relation used in the present work is similar to (24) of Sekelsky et al. (1999) for $\mu = 0$.

The non-Rayleigh scattering term F depends on the thermodynamic phase of the non-Rayleigh scatterers. A temperature profile (obtained, e.g., by radio sounding or by a mesoscale model) is thus useful to implement this computation. At the melting level, the scattering term is interpolated between the values observed at the lower and upper limits of this level. Of course, the measured radar reflectivity factors have to be corrected for the attenuation by gas, notably for W and Ka bands. This is done with data obtained from a radio sounding or from a mesoscale model, and from the radar data for the propagation in the cloud.

The organization of the three-wavelength algorithm is summed up in Fig. 2 where M_w and M_i are written as the liquid water content (LWC) and ice water content (IWC), respectively.

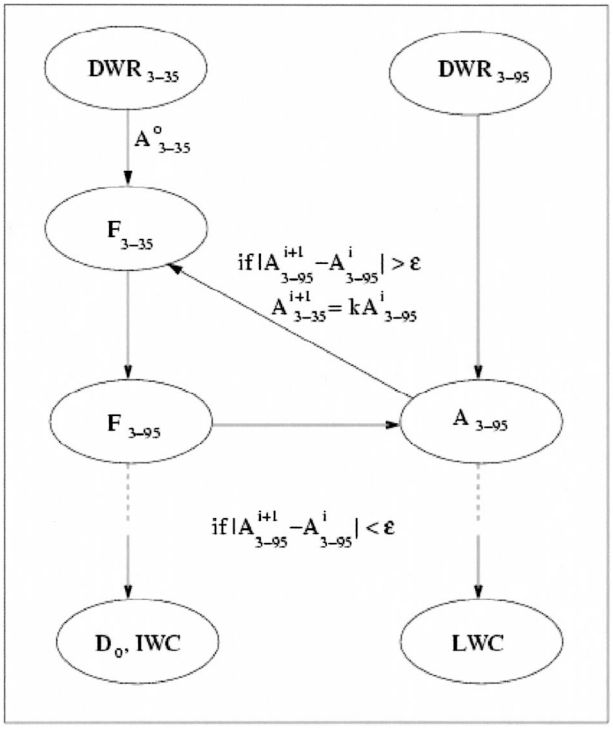

FIG. 2. Schematic of the triple-wavelength radar algorithm for cloud liquid and ice water content and mean volume diameter profiles retrieval. Symbols are defined in section 4a.

b. Simulation

A simulation of the proposed algorithm was implemented for the case of a mixed cloud. The non-Rayleigh scatterers are ice particles. The mixed cloud is assumed to be made up of the superimposition of a non-Rayleigh ice particle distribution and a Rayleigh supercooled droplet distribution. Figure 3 shows the assumed radial variations of the size distribution for the liquid water $M_w(D)$ and ice $M_i(D)$ components. The corresponding reflectivity factor profiles used for the simulation are obtained by resolving the radar equation for Z, for each wavelength, from the radial variation of the size distributions $M_w(D)$ and $M_i(D)$. The backscattering and attenuation cross sections are computed with the Mie scattering model (Deirmendjian 1969). The attenuation by gas is not considered in this simulation.

Figure 4a displays the simulated radial variation of differential attenuation computed from the condition of Fig. 3 for the (S, W) pair as well as $A_{d,SW}$ retrieved from the triple-wavelength method. The agreement between $A_{d,SW}$ assumed and retrieved is satisfactory. Figure 4b displays the radial variation of the liquid water content simulated (i.e., proportional to the derivative with respect to the distance of the simulated differential attenuation $A_{d,SW}$) and retrieved from the dual-wavelength algorithm for the (S, Ka) and (S, W) pairs, and using the triple-wavelength algorithm. These curves show that the triple-wavelength algorithm enables a correct retrieval of the liquid water content variations. As expected, the dual-wavelength method, in the presence of a significant non-Rayleigh component, provides biased results. The (S, W) pair seems slightly better than the (S, Ka) one. Of course, this last remark should be qualified because the W band suffers much more than the

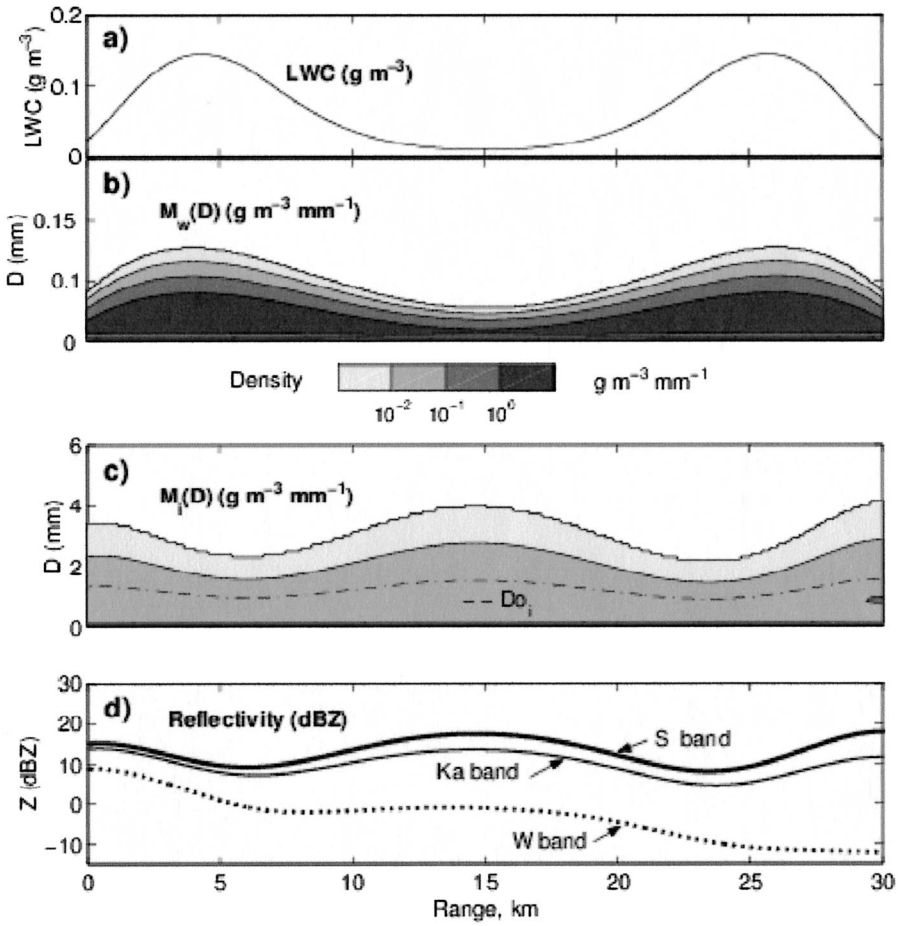

FIG. 3. Assumed radial variation of (a) LWC, (b) size distribution of the droplets $M_w(D)$, (c) size distribution of the ice particles $M_i(D)$, and (d) resulting radial variation of the ''observed'' radar reflectivity factors at S, Ka, and W bands.

Ka band from gaseous attenuation and the limit of extinction. Replacing an S band by an X band (or other wavelength between S and X) as long wavelength does not modify the results (curves for the X band are not given to avoid redundancy).

c. Use on the field data case of 13 April 1999

The triple-wavelength algorithm was applied to the case of 13 April 1999 observed with three radars installed at the Chilbolton Radar Observatory, an experimental site of the Rutherford and Appleton Laboratory managed by the Radio-Communication Research Unit (RCRU), located in the southern part of the United Kingdom, about 100 km west of London (50.1°N, 1.3°W, altitude 80 m). The upper-air data for this case are given in Fig. 5.

The three radars are the CAMRa 3-GHz radar with a 25-m dish (Goddard et al. 1994), the Rabelais 35-GHz radar of the Laboratoire dAérologie (Université Paul Sabatier, France), and the Galileo 94-GHz radar of the European Space Agency. Rabelais and Galileo were set up on the edge of the dish of the CAMRa radar, so that the axes of the beams of the three radars were parallel. The characteristics of the three radars are given in Table 2. The radars were carefully calibrated, the CAMRa from a polarimetric procedure proposed by Goddard et al. (1994), Rabelais and Galileo by comparison with CAMRa. The data from the three radars are interpolated inside a common grid of mesh 100 m × 100 m.

Figure 6 displays the reflectivity factor distribution in range–height indicator (RHI) mode observed with the three radars on 13 April 1999 along the south–southeast direction (163°), on a cluster of cumulus congestus clouds. Three different RHIs corresponding to the three columns of Fig. 6 are presented. The data are corrected for the attenuation by gas with coefficients calculated using radiosonde ascent at 1200 UTC. The three RHIs are separated by about 100 s. The cloud cluster was drifting toward the east, with the general circulation, at a velocity of about 20 m s^{-1}, in such a way that the RHIs approximately represented three parallel planes about 2000 m from each other. The top of the cloud, near 4500 m AGL, was at a temperature of −27°C. The

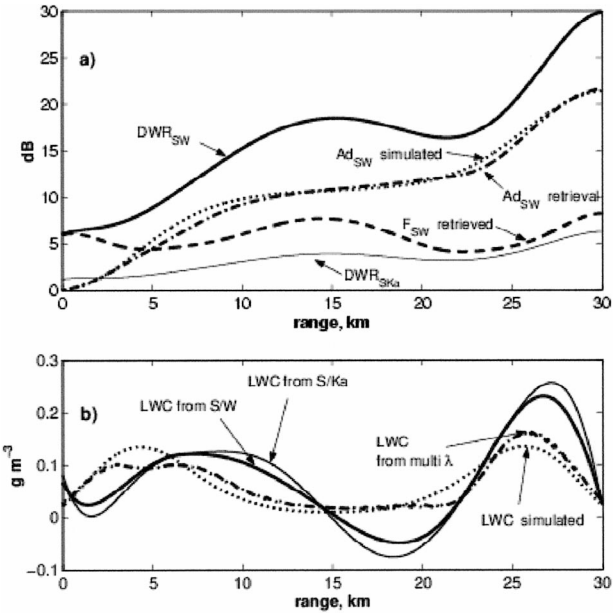

FIG. 4. (a) Simulated radial variation of DWR and differential attenuation, (A_d), for the (S, W) pair and simulated radial variation of DWR for the (S, Ka) pair; Mie scattering term $F_{S,W}$ and differential attenuation $A_{d,SW}$ for the (S, W) pair retrieved with the triple-wavelength algorithm. (b) LWC simulated and retrieved from the dual-wavelength algorithm for the (S, Ka) and (S, W) pairs, and from the triple-wavelength algorithm; the simulated water content to be compared with the retrieved one is obtained by derivating $A_{S,W}$ with respect to the distance.

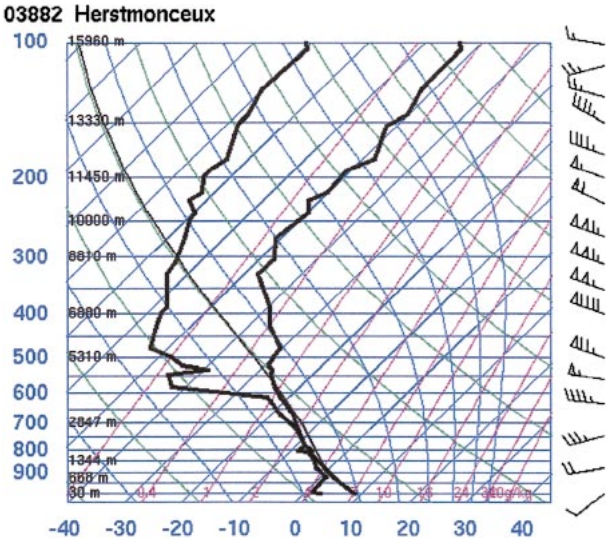

FIG. 5. Radio sounding of Herstmonceux (50.90°N, 0.31°W) on 13 Apr 1999 at 1200 UTC. Abscissa is temperature in °C, ordinate is pressure in hPa. The wind, on the right part, is given in kt with values of 5, 10, 50 for half barb, full barb, and triangle, respectively.

0°C isotherm was near 750 m AGL, but no melting band appears on the reflectivity distribution. The dynamical and microphysical processes involved in such clouds are rather correctly understood (e.g., Young 1993). The absence of melting band suggests that precipitations are made up of granular ice (graupels or snow pellets) as frequently observed in convective clouds. Besides, extinction is only reached in the upper-right part of the 94-GHz panel, showing that the propagation medium is not strongly attenuating. The main difference between the three RHIs is that the convective structure observed at a distance ranging between 5 and 11 km in the left column diminishes and disappears in the middle and right columns, respectively, while the ''wall'' of strong reflectivity observed at 11 km of distance in the left column stands farther away, at a distance near 12 and 15 km, in the middle and right columns. Clearly, what is presented in the three RHIs is a three-dimensional structure in which precipitation shafts can cut the RHI planes (the RHIs are not in the plane of the precipitation shafts since the azimuth is not in the wind direction). In the data used, the width of the radar beams is smaller than 174 m (the beamwidth of the Rabelais radar at 20 km of distance). Figure 7 shows the DWR distributions observed for the (3, 35), (35, 94), and (3, 94) GHz pairs, for the three RHIs of Fig. 6. Figure 8 shows the distributions of the non-Rayleigh scattering term $F_{3,94}$ for the first and last (fourth) steps of the iteration, and the differential attenuation $A_{3,94,}$ for the three RHIs of Fig. 6. Figure 9 gives the distribution of the mean volume diameter (D_0), LWC, and IWC retrieved with the triple-wavelength algorithm for the three RHIs of Fig. 6.

The differences between the reflectivities observed at the three frequencies (Fig. 6) reveal the dramatic distorsions brought by the attenuation and non-Rayleigh scattering for increasing frequencies. The 3-GHz panel represents the reflectivity field in the absence of attenuation and non-Rayleigh effects. The 35-GHz panel displays a reflectivity distribution in which the larger-size

TABLE 2. Main characteristics of the radars.

	CAMRa	Rabelais	Galileo
Frequency (GHz)	3.075	34.94	94.8
Peak power (kW)	600	50	2
Antenna diameter (m)	25	1.4	0.5
Beamwidth, 3 dB (°)	0.26	0.43	0.5
Pulse width (μs)	0.5	0.3	0.5
Scan rate (° s^{-1})	1	1	1
Pulse repetition frequency (Hz)	610	3125	6250
Noise equivalent reflectivity (at 1 km) (dBZ)	−34	−27	−34

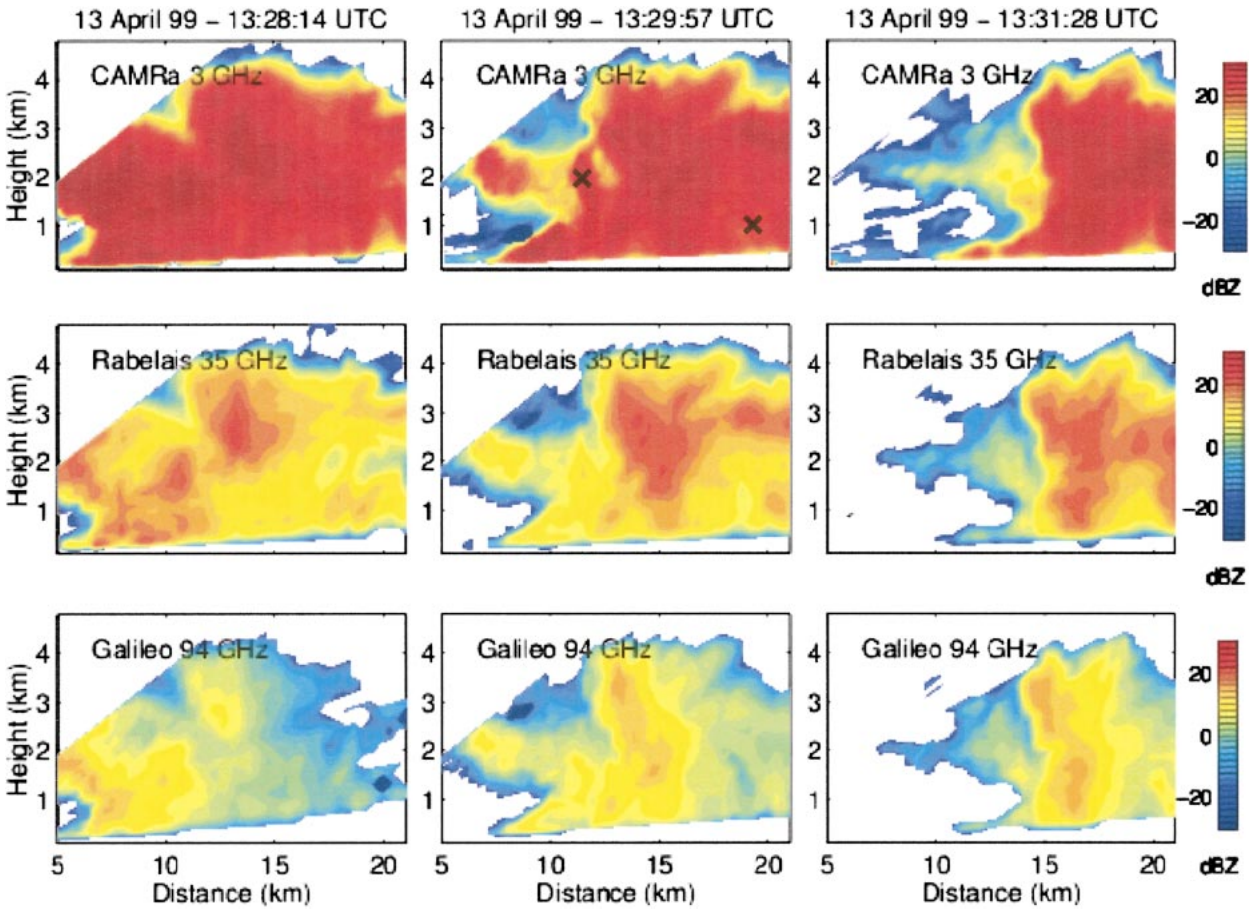

FIG. 6. Reflectivity factor distribution observed in RHI mode with the three radars on 13 Apr 1999, at (left) 1328:14, (middle) 1329:57, and (right) 1331:28 UTC.

scatterers do not correspond to the areas of maximum reflectivities. A striking example is that of the areas of maximum D_0 appearing in the upper-left panel of Fig. 9, notably at a distance between 5 and 10 km and a height of 1.5 and 2.5 km in the left column. This maximum does not appear at 35 GHz in the left column of Fig. 6. On the 94-GHz panel, the reflectivity distribution is even further damaged with, in addition, a very strong gradient of attenuation.

Figure 7 emphasizes these distorsions. Because 35 GHz is not strongly attenuated (compared to 94 GHz; cf. Table 1) over short distance, high values of $\mathrm{DWR}_{3,35}$ display mainly non-Rayleigh effects associated with the distribution of large scatterers (non-Rayleigh effects become significant for scatterers larger than about 2 and 1 mm at 35 and 94 GHz, respectively). In the $\mathrm{DWR}_{35,94}$ row of Fig. 7, the attenuation effects at 94 GHz are dominant and the ratio increases regularly with the distance, with the stronger gradients in the upper-right part. The $\mathrm{DWR}_{3,94}$ panels display the addition of the two previous distributions. The non-Rayleigh effects are dominant at short distances in the left part of the panels and the attenuation is dominant in the right part. The high values appearing at the lower boundary of bottom-left panel of Fig. 7 ($\mathrm{DWR}_{3,94}$ for 13 April 1999) are an artifact due to an edge effect.

Figure 8, the distribution of the backscattering term without attenuation for the pair (3, 94) GHz, shows the efficiency of the iterative process. For the last step of iteration $F_{3,94}(D_0)$ retrieves a distribution qualitatively mirroring the D_0 repartition of Fig. 9, upper row. In order to visualize the efficiency of the iterative process, Fig. 10 shows the evolution of the difference $|A_{ls}^{i+1} - A_{ls}^{i}|$ at the end of the radials for the successive steps (or iteration). The largest differences are observed in the presence of non-Rayleigh scatterers. The condition $|A_{ls}^{i+1} - A_{ls}^{i}| < \varepsilon$, with $\varepsilon = 0.5$ dB, is satisfied after four steps. In Fig. 8, the lower row displays the distribution of the (3, 94) GHz pair cumulative attenuation. The cumulative attenuation diminishes with the disappearance of the left-part-convective structure.

In Fig. 9, the upper row presents the retrieved mean volume diameter of the scatterers (D_0). The distribution is patchy because the precipitation shafts cross the plane of the RHI scans. The LWC (i.e., M_w) distribution in the middle row of Fig. 9 retrieves the area of maximum

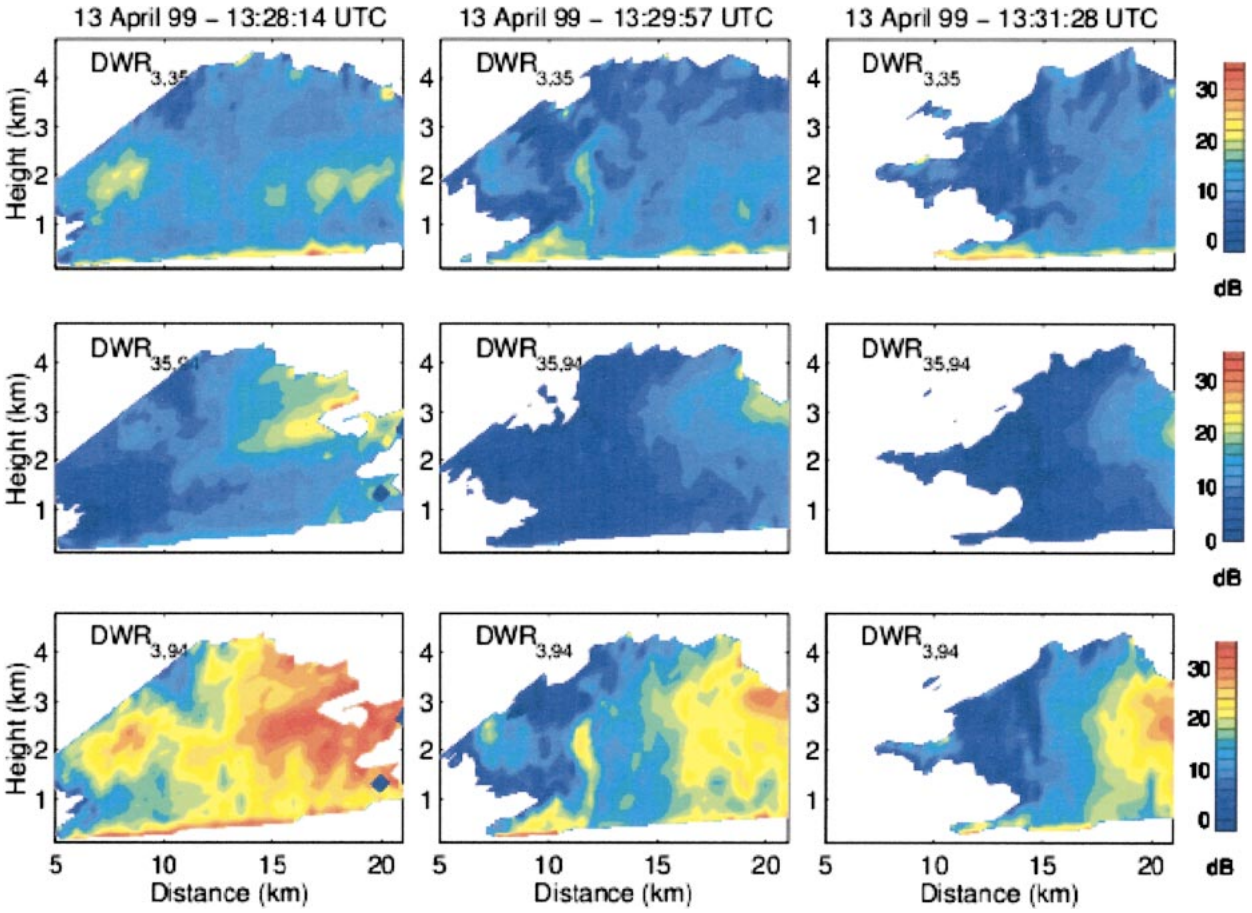

FIG. 7. DWR for the (3, 35), (35, 94), and (3, 94) GHz pairs for the three RHIs of Fig. 6.

values where the updrafts generating the precipitation in cumulus clouds can be expected, in the upper part of the clouds, at the head of the precipitation structure. In such convective cells, the updrafts are usually strong enough to create supercooled water clouds inside the ice clouds because the deposition on the ice crystals does not totally consume the water vapor released by the air ascent (e.g., Young 1993). The IWC (i.e., M_i) distribution is presented in the lower row of Fig. 9. Ice is present in all parts of the cloud with highest IWC values associated with the precipitation. The two areas of high D_0 are not associated with high IWC, suggesting that they are made up of large particles with low numerical concentration and low IWC.

To validate the distribution of Fig. 9, simultaneous in situ microphysical measurements would be necessary. Such data are not available. However, qualitative considerations suggest that the retrieved distributions are reasonable and realistic.

d. Practical aspects of implementation

The three radars have to sample the same volume in the same conditions. All the terms that might decorrelate the measurement of the three radars are thus expected to corrupt the accuracy of the three-wavelength radar algorithm. Of paramount importance is the matching of the three radar beams; that is why it is preferable to set up the three radar antennas on the same pedestal. The pulse volumes, range bin distances, and dwell times have to be the same.

A careful calibration of the three radars is necessary. As an example of sensitivity to calibration, Fig. 11 shows the change of D_0, LWC, and IWC, with respect to the value of Fig. 9, resulting from an error on the reflectivity measurements at 35 and 94 GHz, that is, Z_{35} and Z_{94}, respectively. The influence of using, for the ice particle density, a function different from (11) is also shown. The curves in Fig. 11 represent the variation with distance of the three parameters for the constant height of 2500 m AGL in the RHI of 1329:57 UTC. For the three parameters, the shift induced in the results by an error in Z can be positive or negative due to the non-Rayleigh response of the large scatterers. Of course, the errors considered independently in Fig. 11 can arise simultaneously giving cumulative effects that can be additive or subtractive. These errors can significantly corrupt the results, suggesting that a calibration error

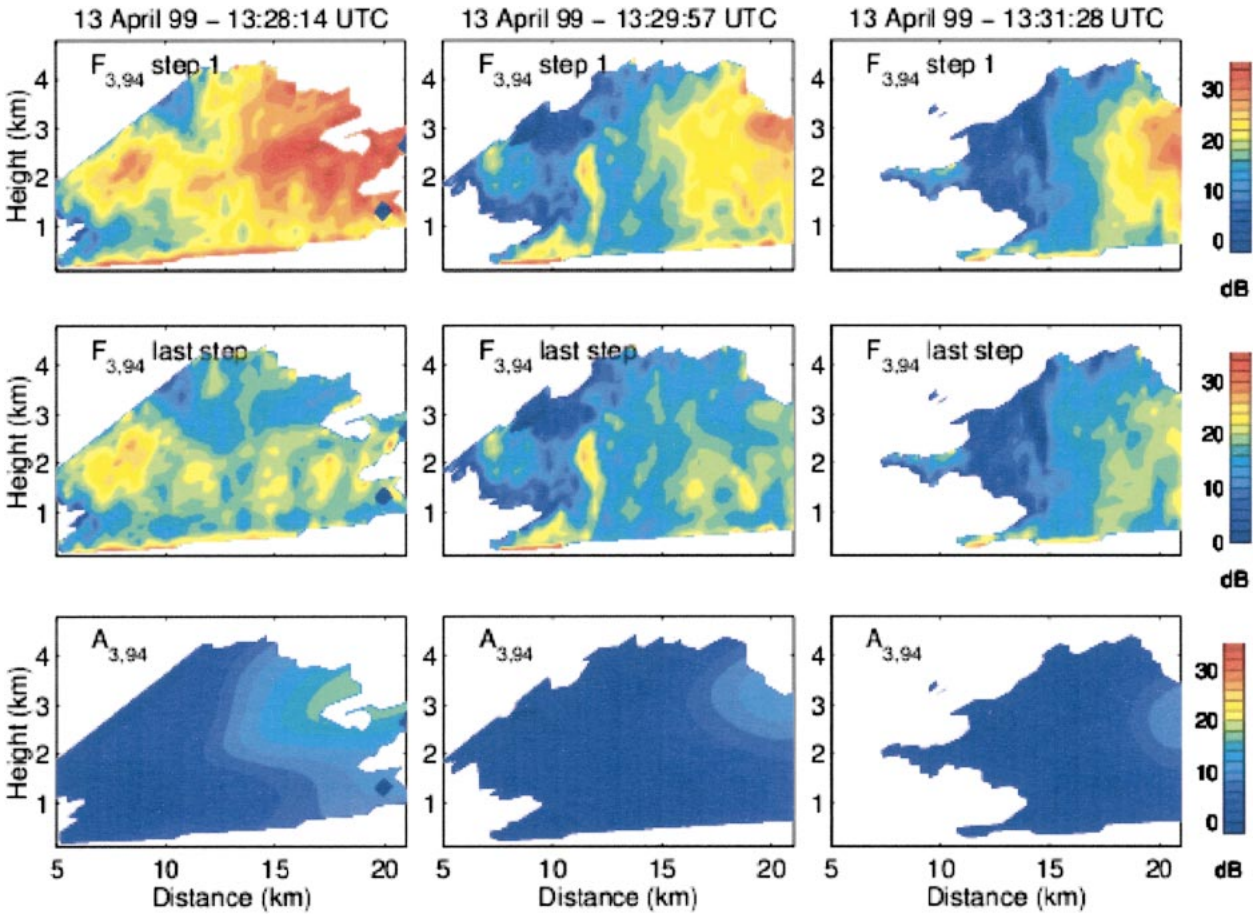

FIG. 8. Distributions of $F_{3,94}$ for the first and last steps of the iteration and differential attenuation $A_{3,34}$, for the three RHIs of Fig. 6.

not worse than ± 1 dB is required. However, D_0 and LWC only depend on the relative calibration of the radars, while IWC depends on the absolute calibration. The error due to the change in the coefficient of the ice density function appears rather strong in Fig. 11 for the three computed parameters; however, the test is for a linear coefficient of the density function reduced by 5 (from 0.916 to 0.175), which is very large. For moderate variations of the coefficients, the changes will be moderate for D_0 and IWC, and almost negligible for LWC.

The optimization of the choice of the three wavelengths, because it influences the signal-to-noise ratio and the resolution of the retrieved distributions (e.g., Gosset and Sauvageot 1992), is also to be considered, as well as the maximum observable distance, which depends on λ_s.

However, the accuracy also depends on the particular conditions of the observation, namely, spaceborne, airborne (and in this case from above or below the melting band), or ground-based radars. Last, the accuracy of the results is contingent on the genus and structure of the clouds observed (stratiform, convective, or mixed, with low or high reflectivity).

A complete study of the accuracy and sensitivity of the proposed method to all these terms, although useful for its evaluation, is out of the scope of the present paper.

5. Conclusions

In the presence of non-Rayleigh scatterers, dual-wavelength methods for liquid water content retrieval in warm and mixed clouds are biased. The reliability of the results depends in fact on the importance of the non-Rayleigh scattering term $F_{\lambda_l,\lambda_s}(D_0)$ with respect to the cumulative differential attenuation $A_d\Delta r$. The present paper suggests that favorable conditions for the use of a dual-wavelength method are not very frequent in nature, notably in mixed clouds where ice crystals are usually large. That is why a triple-wavelength radar method is proposed to overcome these difficulties.

In this method, a long wavelength (λ_l), a medium one (λ_m), and a short one (λ_s) are considered in order to observe two dual-wavelength ratios, one ($\mathrm{DWR}_{l,m}$) with low differential attenuation and the other ($\mathrm{DWR}_{l,s}$) with high differential attenuation. Using $\mathrm{DWR}_{l,m}$observations and ignoring the differential attenuation, a first estimate of the D_0 profile is computed. With this profile and $\mathrm{DWR}_{l,s}$observations, an estimate of the cumulative ra-

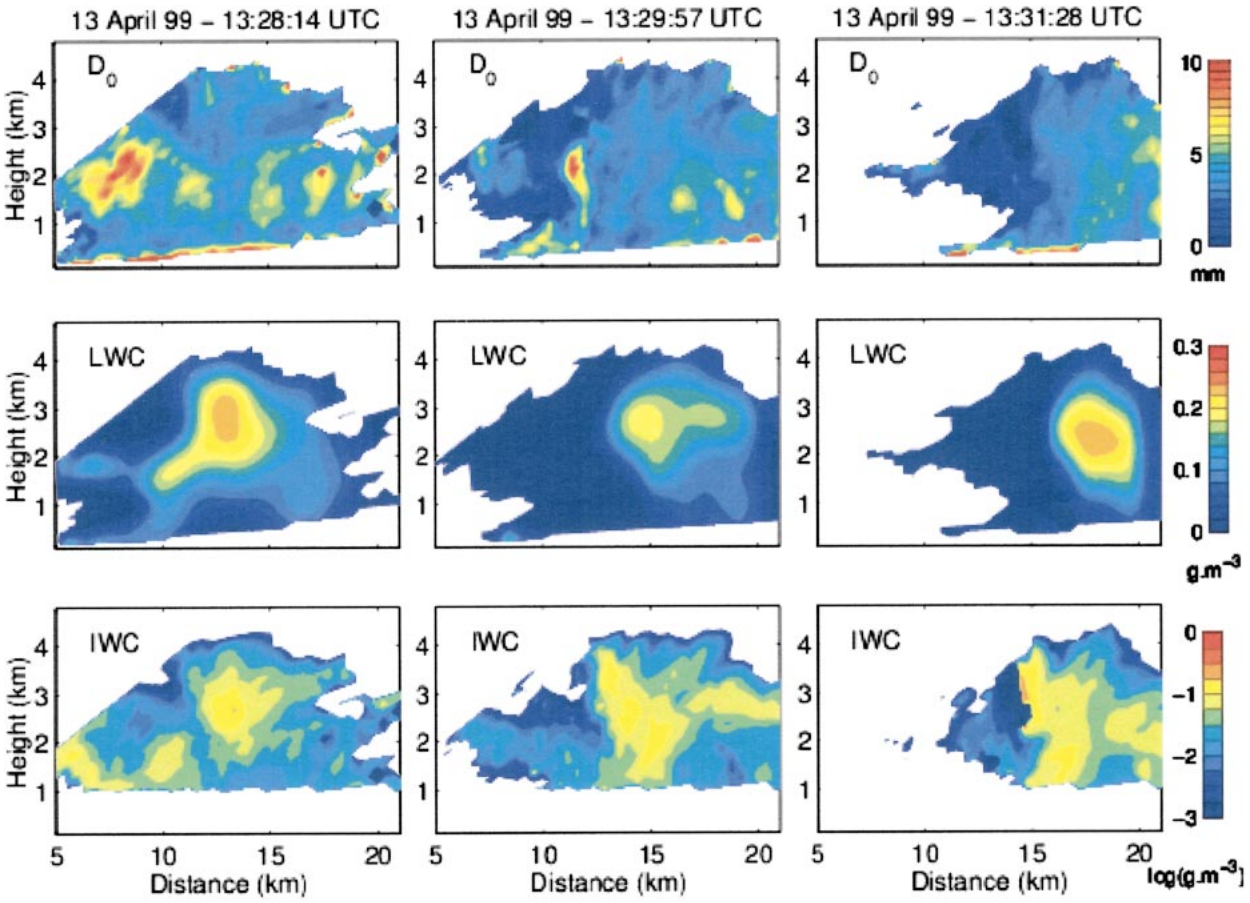

FIG. 9. Mean volume diameter of scatterers (D_0), LWC, and IWC retrieved with the triple-wavelength algorithm for the three RHIs of Fig. 6.

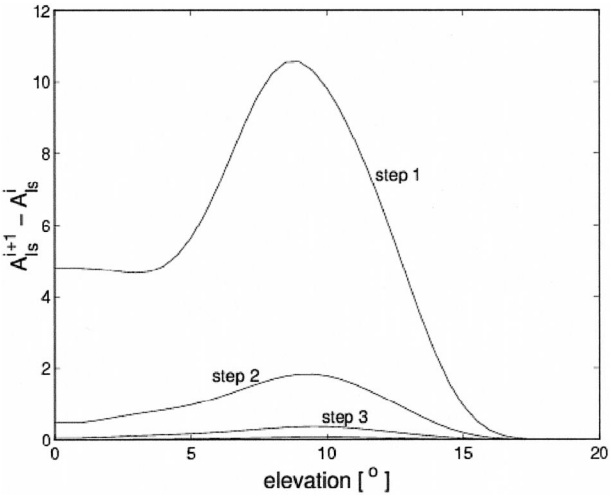

FIG. 10. Variation of residual attenuation $A_{ls}^{i+1} - A_{ls}^{i}$ in dB, as a function of the elevation angle of the radar beams for the successive iterative steps of the triple-wavelength algorithm.

dial variation of A_d is computed. From this, an estimate of the differential attenuation A_d affecting the $\mathrm{DWR}_{l,m}$ profile is obtained. Then, from the $\mathrm{DWR}_{l,m}$ and the A_d profiles, a new more exact D_0 profile is computed, and so on until obtaining stable LWC, IWC, and D_0 profiles.

Simulation and field observations processing using the λ_s–λ_{Ka} and λ_s–λ_w wavelength pairs are presented. The three wavelengths suggested for the implementation of this method are λ_x or higher for the long wavelength and λ_{Ka} and λ_w for the medium and short wavelengths, respectively. The results show that the proposed method has an interesting potential to retrieve the profile of the liquid water content and the mean volume diameter of the non-Rayleigh component in mixed phase or in warm clouds.

Acknowledgments. We thank the Radio-Communication Research Unit at the Rutherford Appleton Laboratory for providing the 3-, 35-, and 94-GHz radar data. We are grateful to Dr. Robin Hogan of the University of Reading for his helpful remarks regarding data analysis and radar calibration. The 1994 Galileo radar was developed for the European Space Agency by Officine

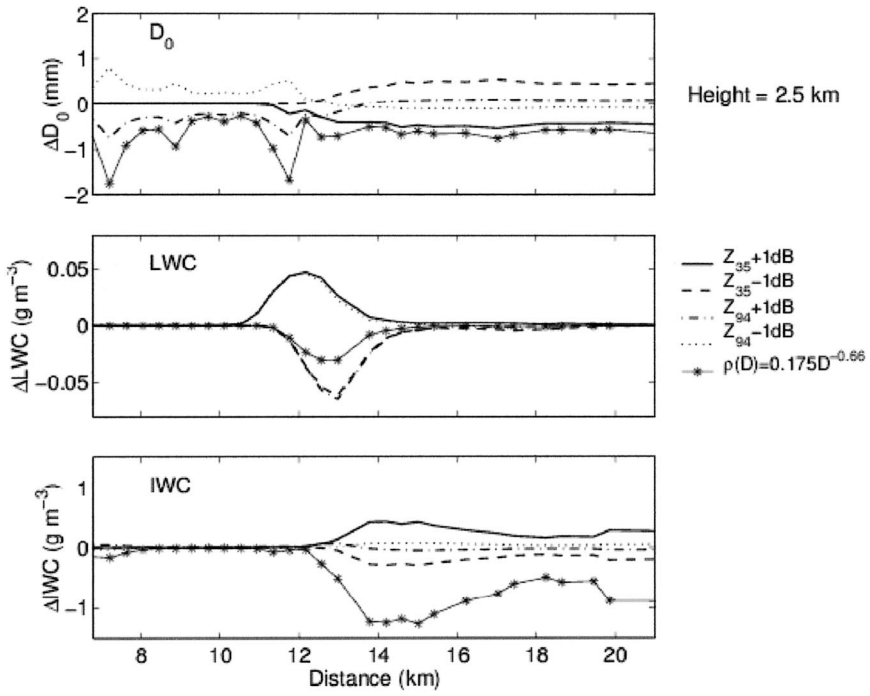

FIG. 11. Variation with distance of the three retrieved parameters D_0, LWC, and IWC resulting from a calibration error of ± 1 dB on Z_{35} and Z_{94}, and from a change in the coefficients of the ice density $\rho(D)$ formula. The curves are for a constant height of 2500 m AGL and the RHI scan of 1329:57 UTC.

Galileo, the Rutherford Appleton Laboratory, and the University of Reading, under NERC Grant GR3/13195 and EU Grant CVK2/CT/2000/00065.

REFERENCES

Atlas, D., 1954: The estimation of cloud parameters by radar. *J. Meteor.*, **11,** 309–317.

——, and F. H. Ludlam, 1961: Multi-wavelength radar reflectivity of hailstorms. *Quart. J. Roy. Meteor. Soc.*, **87,** 523–534.

Brown, P., and P. Francis, 1995: Improved measurements of ice water content in cirrus using a total water probe. *J. Atmos. Oceanic Technol.*, **12,** 410–414.

Cess, R. D., and Coauthors, 1996: Cloud feedback in atmospheric general circulation models: An update. *J. Geophys. Res.*, **101,** 12 761–12 795.

Deirmendjian, D., 1969: *Electromagnetic Scattering on Spherical Polydispersion.* Elsevier, 290 pp.

Eccles, P. J., and E. A. Muller, 1971: X-band attenuation and liquid water content estimation by dual-wavelength radar. *J. Appl. Meteor.*, **10,** 1252–1259.

——, and D. Atlas, 1973: A dual wavelength radar hail detector. *J. Appl. Meteor.*, **12,** 847–854.

Fox, N. I., and A. J. Illingworth, 1997: The retrieval of stratocumulus cloud properties by ground-based cloud radar. *J. Appl. Meteor.*, **36,** 485–492.

Goddard, J. W. F., J. Tan, and M. Thurai, 1994: Technique for calibration of meteorological radars using differential phase. *Electron. Lett.*, **30,** 166–167.

Gosset, M., and H. Sauvageot, 1992: A dual-wavelength radar method for ice–water characterization in mixed-phase clouds. *J. Atmos. Oceanic Technol.*, **9,** 538–547.

Hogan, R. J., and A. J. Illingworth, 1999: The potential of spaceborne dual-wavelength radar to make global measurements of cirrus clouds. *J. Atmos. Oceanic Technol.*, **16,** 518–531.

——, ——, J. W. Goddard, S. C. Jongen, and H. Sauvageot, 1999: Stratocumulus liquid water content from dual wavelength radar. *Int. Workshop Proc. CLARE '98 Cloud Lidar and Radar Experiment,* Noordwijk, Netherlands, ESA, ESTEC, 197–109.

——, ——, and H. Sauvageot, 2000: Measuring crystal size in cirrus using 35- and 94-GHz radars. *J. Atmos. Oceanic Technol.*, **17,** 27–37.

Martner, B. E., R. A. Kropfli, L. E. Ash, and J. B. Snider, 1993: Dual-wavelength differential attenuation radar measurements of cloud liquid water content. Preprints, *26th Int. Conf. on Radar Meteorology,* Norman, OK, Amer. Meteor. Soc., 596–598.

Meneghini, R., and T. Kozu, 1990: *Spaceborne Weather Radar.* Artech House, 197 pp.

Ray, P. S., 1972: Broadband complex refractive indices of ice and water. *Appl. Opt.*, **11,** 1836–1844.

Sauvageot, H., 1992: *Radar Meteorology.* Artech House, 366 pp.

——, and J. Omar, 1987: Radar reflectivity of cumulus clouds. *J. Atmos. Oceanic Technol.*, **4,** 264–272.

Sekelsky, S. M., W. L. Ecklund, J. M. Firda, K. S. Gage, and R. E. McIntosh, 1999: Particle size estimation in ice-phase clouds using multifrequency radar reflectivity measurements at 95, 33, and 2.8 GHz. *J. Appl. Meteor.*, **38,** 5–28.

Stephens, G. L., S. C. Tsay, P. W. Stakhouse, and P. J. Flatan, 1990: The relevance of microphysical and radiative properties of cirrus clouds to climate and climatic feedback. *J. Atmos. Sci.*, **47,** 1742–1752.

Ulaby, F. T., R. K. Moore, and A. K. Fung, 1981: *Microwave Remote Sensing.* Vol. 1. Addison-Wesley, 456 pp.

Vivekanandan, J., B. Martner, M. K. Politovich, and G. Zhang, 1999: Retrieval of atmospheric liquid and ice characteristics using dual-wavelength radar observations. *IEEE Trans. Geosci. Remote Sens.*, **37,** 2325–2334.

Young, K. C., 1993: *Microphysical Processes in Clouds.* Oxford University Press, 427 pp.